Metal-organic framework derived multi-functionalized and co-doped TiO$_2$/C nanocomposites for excellent visible-light photocatalysis

Mian Zahid Hussain [a,b], Zhuxian Yang [a], Ahmed M.E. Khalil [a,c], Shahzad Hussain [d], Saif Ullah Awan [e], Quanli Jia [f], Roland A. Fischer [b], Yanqiu Zhu [a], Yongde Xia [a,*]

[a] *College of Engineering, Mathematics and Physical Sciences, University of Exeter, Exeter EX4 4QF, United Kingdom*

[b] *Department of Chemistry and Catalysis Research Centre, Technical University of Munich, Garching, 85748, Germany*

[c] *Department of Chemical Engineering, Faculty of Engineering, Cairo University, Giza 12613, Egypt*

[d] *Department of Physics, COMSATS University Islamabad, 45550, Pakistan*

[e] *Department of Electrical Engineering, National University of Sciences and Technology, Islamabad, Pakistan*

[f] *Henan Key Laboratory of High Temperature Functional Ceramics, Zhengzhou University, Zhengzhou, 450052, China*

* Corresponding author.

E-mail address: Y.Xia@exeter.ac.uk (Y. Xia).

ABSTRACT

Multi-functionalized and co-doped TiO_2/C nanocomposites derived from the pyrolysis of Ti-MOFs at 800 °C under different gaseous atmospheres were produced and their photocatalytic performance were investigated. The gaseous atmosphere during pyrolysis plays a critical role in determining the structural, textural, optical and physicochemical properties of the derived TiO_2/C composites, due to the synergistic effects of nitrogen-containing species, carboxylate and/or sulfur functionalized porous carbons and N/S co-doped TiO_2 nanoparticles. All the Ti-MOFs derived TiO_2/C composites exclusively possess homogeneously distributed TiO_2 nanoparticles in functionalized disc-like porous carbon matrix and demonstrate much enhanced adsorption and photodegradation performance than commercial TiO_2 under the same conditions. The adsorption and degradation of methylene blue (MB) in dark on these TiO_2/C composites are dominated with pseudo second-order kinetic model and the high adsorption and degradation capacity of MB in dark on composite TiO_2/C derived from MIL-125(Ti) in argon is due to its high surface area with predominant mesoporous carbon matrix in the composite. The composite N-O-TiO_2/C derived from NH_2-MIL-125(Ti) in water vapor exhibited the highest photodegradation activity with 99.7% MB removal in 3 hours under visible light due to the optimal anatase/rutile phasejunction, together with the formation of photoactive oxygen-rich N-O like interstitial/intraband states above the valence band of TiO_2, as well as the presence of rich N-containing species and -OH/-COOH multi-functional groups with superhydrophilic nature of the composite. This simple one-step and easily modifiable approach can be further employed to modulate many homogeneously dispersed multi-functionalized and co-doped metal oxide/carbon nanocomposites for various environment and energy-related applications.

1. Introduction

The continuous release of toxic organic pollutants such as industrial waste materials, textile dyes and pharmaceutical contaminants are causing severe water pollution at a global scale. Many of these industrial pollutants are difficult to filter and recycle through conventional filtration systems. Therefore, it is of utmost importance to develop new strategies for the treatment of industrial wastes to prevent it from continuously polluting the water sources. Photocatalytic decomposition of organic pollutants using the sunlight has been proved to be a viable solution to mineralize the toxic contaminants in wastewater [1]. The photodegradation of organic pollutants involves the sunlight as a source of energy and a semiconducting material with appropriate energy band gap as a photocatalyst to carry out the photocatalytic redox reaction to decompose the toxic molecules into benign species such as CO_2 and H_2O [1-5].

A large variety of transition metal semiconducting materials such as TiO_2 can be utilized as photocatalysts [6, 7]. However, due to the wide energy band gap of TiO_2 (3.2 - 3.0 eV), it only absorbs the UV light which consists of 5% of the solar spectrum. However, the photocatalytic efficiencies of the photocatalytic materials can be significantly improved if the photocatalyst could absorb light in visible region which comprises around 43% of the solar spectrum. Several strategies have been successful developed to narrow the energy band gap of semiconducting TiO_2 including the doping of metallic and/or non-metallic species, the formation of heterojunctions, as well as the generation of defects [7-16]. However, other challenges, such as the inaccessibility of the photocatalytic active sites due to the formation of agglomerates of TiO_2 nanoparticles, inevitably limit the photodegradation performance of the photocatalysts. Therefore, various methods have been tried to improve the accessibility of the active sites and to prevent the formation of agglomerate by mixing TiO_2 with carbon i.e., graphene or porous carbon to form composites [17-20]. Although the metal oxide/carbon composites demonstrated improved photocatalytic performance, the composites produced via

physical and mechanical mixing methods usually result in a non-uniform distribution of metal oxides on graphitic carbon and poor textural properties with limited enhancement in photocatalytic performance [21-23]. A promising and high performing photocatalyst should demonstrate modifiable textural, optical and surface properties. Obviously, the pore sizes and pore shapes of the photocatalysts with high surface area should be appropriate to accommodate the organic pollutants. Moreover, the hydrophilic/hydrophobic nature of surface-attached functional groups also play a significant role in maximizing the interaction between organic pollutants and the photocatalyst [14, 24]. Clearly, the TiO_2/C composites obtained via the conventional routes lack such synergistic properties.

The past 10 years have witnessed enormous growth in the metal-organic frameworks (MOFs) derived materials for a large variety of applications in various fields including environment and energy [25-27]. MOFs consist of metal ions and organic linkers, bound together by the coordination bonds to form highly porous polymeric structures [28-31]. Their distinct features such as high crystallinity, modifiable morphologies, tunable textural properties and easily surface functionalization make them exceptional materials to be used as precursors and sacrificial templates to generate porous metal oxide/carbon composites [3, 26, 32]. MOFs derived composites offer a combination of tunable properties such as physicochemical, structural, optical and textural properties which play a critical role in the adsorption and photodegradation of organic pollutants. The surface-attached functional groups act as trapping centres and the open pore networks with appropriate pore shapes and sizes facilitate the diffusion of organic dye molecules into the micro/mesopore channels and access to active sites of metal oxide photocatalysts [33-35]. It is believed that during the photodegradation of organic pollutants, the visible light irradiation generates electron−hole pairs in semiconducting metal oxides. The photoinduced electrons (e^-) jump to the conduction band and react with oxygen presented in the water, producing superoxides ($O_2 \cdot^-$); whereas the photoinduced holes (h^+) in

valence band form hydroxyl (•OH) radicals via water oxidation. The reduction of organic dye is induced by O_2•$^-$, whereas the •OH radicals oxidize the organic dye molecules, leading to their mineralization [2, 23, 36, 37]. Though a few studies on MOF derived TiO_2/C composites for photocatalysis have been reported, to the best of our knowledge, no detailed study is available on the Ti-MOF derived multi-functionalized and co-doped TiO_2/C composites for photocatalytic activity [37-39].

Herein, the role of functional groups and non-metal dopants in MIL-125(Ti) and NH_2-MIL-125(Ti) derived multi-functionalized and co-doped TiO_2/C nanocomposites for the adsorption and photodegradation of organic dye methylene blue (MB) is investigated in this study. This work provides a novel insight about the synergistic effects of nitrogen, carboxylate and/or sulfur functionalized porous carbon and N and/or sulfur co-doped TiO_2 nanoparticles on photocatalytic performance of the Ti-MOF derived nanocomposites. Based on the in-depth characterizations and photodegradation evaluation of TiO_2/C based composites, this study suggests that the presence of -N, -OH/-COOH and/or S functional species in the composite play a significant role in determining the crystalline phase growth of TiO_2, the surface areas and pore sizes, the energy band gaps (via non-metal doping) and the hydrophilic properties of the composites. The adsorption and degradation of methylene blue (MB) in dark on these TiO_2/C composites are dominated with pseudo second-order kinetic model and the high adsorption capacity of MB by the composite TiO_2/C in dark is attributed to the high surface area porous carbon matrix in the composite. Whereas the highest photodegradation of MB under visible light is due to the optimal anatase/rutile phasejunction and the formation of photoactive oxygen-rich N-O like interstitial/intraband states above the valence band of TiO_2, as well as the rich -OH/-COOH functional groups with superhydrophilicity of the composite.

2. Experimental

2.1. Synthesis of MIL-125 and NH$_2$-MIL-125(Ti)

The synthesis method of NH$_2$-MIL-125(Ti) is reported in our recently published work [40]. Briefly, 30 mM (5.43 g) of 2-aminoterephthalic acid (NH$_2$-BDC) was added into 100 mL solution of dimethylformamide (DMF) and methanol (MeOH) (with 1:1 volumetric ratio) in a 200 mL glass bottle and stirred for 15 min at room temperature. Once fully dissolved, 7.3 mM (2.47 mL) of Ti(OBu)$_4$ was added into this solution under constant stirring for 10 minutes and then transferred the glass bottle to an oil bath at 130 ºC for 40 hours. The yellow crystalline powder of NH$_2$-MIL-125(Ti) was separated from the solvent by centrifugation, followed by washing twice with the fresh DMF to remove all the unreacted species. The same washing procedure was repeated twice with the MeOH for solvent exchange. The collected NH$_2$-MIL-125(Ti) was dried at 70 ºC in air overnight. The MIL-125(Ti) was also prepared via the same procedure by using terephthalic acid (BDC) as an organic linker.

2.2. Synthesis of MIL-125(Ti) and NH$_2$-MIL-125(Ti) derived multi-functionalized co-doped TiO$_2$/C

The multi-functionalized and co-doped TiO$_2$/C nanocomposites were obtained by simple one-step direct pyrolysis of the as-synthesized MIL-125(Ti) and NH$_2$-MIL-125(Ti) at 800 ºC under different gaseous atmospheres such as argon (Ar), water vapor (H$_2$O) and hydrogen sulfide (H$_2$S). For each sample, an alumina boat loaded with 750 mg of as-prepared MIL-125(Ti) was placed in a flow-through quartz tube furnace connected to Ar gas with the flow rate set at 50 mL min^{-1}. The heating ramp rate of the tube furnace was adjusted at 5 °C min^{-1} with the dwell time of 2 hours at the target temperature. The nanocomposite obtained from the carbonization of MIL-125(Ti) under Ar is named as **TiO$_2$/C.** The second sample was prepared by carbonization of NH$_2$-MIL-125(Ti) under Ar at 800 °C. This N-functionalized TiO$_2$/C

composite is designated as **N-TiO₂/C**. The third sample with N and S functionalities on the surface of porous carbon was obtained by the pyrolysis of NH_2-MIL-125(Ti) under a mixture of H_2S and Ar gas. This composite is named as **N-S-TiO₂/C**. To functionalize the porous carbon surface of the derived TiO_2/C composite with N and oxygen-rich carboxylate (-COOH) groups, water vapor were introduced at the target temperature 800 °C with dwell time for 2 h. The introduction of water vapor into the tube furnace was realized by passing Ar gas through a water buffer bottle to carry the saturated water vapor before entering the tube furnace. This composite is labelled as **N-O-TiO₂/C**. The commercially available TiO_2 (P-25), labelled as **Comm. TiO₂** was taken as a reference sample for the comparison of photocatalytic dye degradation activity under visible light.

2.3. Material characterizations

Powder X-ray diffraction (PXRD) patterns of as-prepared NH_2-MIL-125(Ti) and the derived nanocomposites were measured by Bruker D8 instrument with Cu Kα radiation (1.54 Å) (40 kV, 40 mA). Rietveld refinement of PXRD data was done using the General Structure Analysis System (GSAS+EXPGUI). The Bragg diffraction peaks were described by pseudo-Voigt a function, which is an approximation for the Voigt function and is a convolution of Gaussian and Lorentzian functions. The background was modeled with a shifted Chebyshev function with ten terms. Thermogravimetric analysis (TGA) coupled with mass spectrometer (MS) profiles were recorded using *Mettler Toledo* TGA/DSC 3 apparatus with a continuous heating ramp rate of 10 °C min⁻¹ under synthetic airflow. The morphologies of the samples were recorded using xT Nova Nanolab 600 FIB coupled with in-situ imaging all in one unit. Transmission electron microscopy (TEM) (JEM 2100 LeB6 200 KV) coupled with energy-dispersive X-ray spectroscopy (EDX) were employed for record TEM images and elemental mappings of the composites. Fourier-transform infrared (FTIR) spectra were recorded using a Bruker Optics Tensor-27 FTIR spectrometer in the range of 4000-400 cm⁻¹. The Raman spectra

were measured using a Renishaw inVia Reflex Raman System RL532C, Class 3B. The laser wavelength is 532 nm with laser power 1%. N_2 gas sorption analysis was carried out at 77 K on a *Quantachrome* Autosorb iQ2 ASiQwin apparatus equipped with a micropore port (1×10^{-5} bar) via the conventional volumetric technique. The surface area of the samples was calculated via BET method based on the adsorption branch data. The pore size distribution (PSD) of the composites was also calculated using non-local density functional theory (NLDFT) method from the adsorption branch data. The surface chemical analysis (XPS) was obtained by the Kratos Axis Ultra DLD spectrometer with a monochromated Al $K\alpha$ X-ray source operating at 168 W (12 mA $\times$ 14 kV). Data were collected with pass energies of 160 eV for survey spectra, and 20 eV for high-resolution scans with step sizes of 1 eV and 0.1 eV respectively.

2.4. Evaluation of adsorption and photodegradation activity

To investigate the role of surface functionalization and non-metal doping of Ti-MOF derived TiO_2/C composites in photocatalytic degradation of organic pollutants, adsorption and photodegradation of methylene blue (MB) were measured in dark and under visible light irradiation respectively. The adsorption of MB by nanocomposites was carried out in a dark box which is in a complete absence of light. For photodegradation studies, the visible light was irradiated using 8 lamps (each 20 W) with a light intensity of 120 mWcm^{-2} (PerfectLight, 380 nm $< \lambda <$ 700 nm). Typically, 10 mg of as-prepared TiO_2/C nanocomposite was added into 50 mL MB aqueous solution (20 mg L^{-1}) under constant magnetic stirring at 600 rpm. The UV-Vis absorption spectra were recorded after fixed time intervals by pipetting out 1 mL aliquots to measure the concentration of MB in the solution. The adsorption and photodegradation (D) of MB in aqueous solution (%) are calculated using the following equation:

$$D\ (\%) = \frac{(C_0 - C_t)}{C_0} * 100 \qquad\qquad (1)$$

where D is the adsorption capacity or photodegradation efficiency, C_0 is the initial concentration whereas C_t is the final concentration of MB in water solution after a time interval

8

t. The kinetics of adsorption of MB were also analyzed using pseudo first-order, pseudo second-order, Elovich kinetic and intraparticle diffusion models. The adsorption curves were fitted by using the following equations:

Pseudo first-order equation

$$\ln(q_e\text{-}q_t) = \ln q_e - k_1 t \tag{2}$$

Pseudo second-order equation

$$t/q_t = 1/k_2 q_e^2 + t/q_e \tag{3}$$

Elovich equation

$$q_t = (1/\beta) \ln(\alpha\beta) + (1/\beta)\ln(t) \tag{4}$$

Intraparticle diffusion model equation

$$q_t = k_p t^{1/2} + C \tag{5}$$

where k_1 and k_2 are the rate constants per minute and q_e and q_t in equations 2 and 3 are the adsorption capacities at equilibrium and at time t respectively. In equation 4, α represents the initial adsorption rate (mg g^{-1} min^{-1}) and β indicates the extent of surface coverage of adsorbent (composite) and the activation energy. In equation 5, k_p is intraparticle diffusion rate constant and C is the intercept related to the thickness of the boundary wall.

The active species trapping experiment was performed to quantify the contribution of photoinduced holes (h^+) or hydroxyl radicals ($\cdot OH$) in a photocatalytic oxidation reaction and subsequent photodegradation of MB. For this purpose, prior to the start of photodegradation under visible light, 10 mL of methanol (MeOH) as h^+ scavenger or 2-propanol (IPA) as $\cdot OH$ scavenger was added into the MB solution.

3. Results and discussion

3.1. Structures, compositions and textural properties

The powder X-ray diffraction patterns (PXRD) of as-prepared Ti-MOFs exhibit main diffraction peaks at 2θ of 6.8^0 , 9.7^0 and 11.6^0 (as shown in Fig. S1), confirming the successful

synthesis of MIL-125(Ti) and NH_2-MIL-125(Ti). Using these as-synthesized Ti-MOFs as sacrificial precursors, surface functionalized and co-doped TiO_2/C composites can be readily derived in controlled gas atmosphere at higher temperatures [40, 41]. During the pyrolysis process, the Ti-MOFs decompose and the Ti oxo-clusters transform into self-doped TiO_2 nanoparticles whereas the organic linkers form a porous carbon matrix under inert gaseous atmosphere [42]. Fig. 1a shows the PXRD patterns of the Ti-MOFs derived different TiO_2/C composites. The main X-ray diffraction peaks for anatase (101) and rutile (110) appeared at 2θ of 25.3^0 and 27.3^0 in sample TiO_2/C respectively. As shown in Fig. 1b, the highlighted rutile phase (110) peak was shifted to higher 2θ of 27.43^0 in N-O-TiO_2/C sample and 27.45^0 in sample N-TiO_2/C and N-S-TiO_2/C respectively. The shifts in the XRD peak positions can be attributed to the modification of the crystalline structure by the self-doped N, O and/or S species into the TiO_2 lattice. These non-metal dopant species create defects and oxygen-related vacancies in TiO_2 crystal lattices as well as promoting the growth of rutile phases, where the N species come from the -NH_2 group of organic linkers NH_2-BDC and the O and S were introduced via the water vapor and H_2S gaseous atmosphere respectively [43].

Fig. 1a also presents the Rietveld refinements of PXRD pattern of TiO_2/C composite [44]. A good agreement between the experimental measurements and refined data was observed. All the parameters were allowed to refine simultaneously once it was estimated that the model was stable. The small values of R parameters (R_{wp} and R_p) and $\chi^2 \approx 1$ as shown in Table S1 indicate that the model was a good approximation of the true structure of derived composites. The weight fraction (%) of anatase and rutile phases in the derived composites was calculated using quantitative Rietveld refinement. Under an argon atmosphere at 800^0 C, MIL-125(Ti) decomposed, forming of 53% well crystalline anatase phase with main diffraction peak at (101) and 47% of rutile phase with main diffraction peak at (110) in sample TiO_2/C. However, the thermal decomposition of NH_2-MIL-125(Ti) under the same pyrolysis conditions

resulted in the formation of N-TiO$_2$/C composite containing 36% crystalline anatase and 64% rutile phase. Introducing water vapor as a mild oxidation source at the target temperature of 800 ^{0} C, the resulting sample N-O-TiO$_2$/C composite derived from the decomposition of NH$_2$-MIL-125(Ti) exhibited 34% of anatase phase and 66% of rutile phase. Interestingly, if NH$_2$-MIL-125(Ti) precursor is pyrolysed in H$_2$S gaseous atmosphere where H$_2$S was introduced along with the argon gas, the formed sample N-S-TiO$_2$/C composite is pronouncedly 74% of rutile phase of TiO$_2$ together with 26% of anatase phase. Frequently, carbon, sulfur and even nitrogen species in the system can act as reducing agents and influence the localized chemical environment, which consequently promote the phase transformation from anatase to rutile phase, due to the doping of these heteroatoms into anatase lattice and forming defects and oxygen vacancies in the resulting composites. In these studied samples, the content of the rutile phase (as shown in Table S1) are estimated to be 47, 64, 66 and 74 % for samples TiO$_2$/C, N-TiO$_2$/C, N-O-TiO$_2$/C and N-S-TiO$_2$/C respectively. A clear trend can be observed that the presence of multiple reducing agents C and N (from the organic linker NH$_2$-BDC) and S (from H$_2$S gaseous atmosphere) promotes the formation of higher content of rutile phase than anatase phase in these samples..[43] Obviously, the pyrolysis gaseous atmosphere of the precursors plays a very important role in the formation of different level of crystalline phases of MOF derived TiO$_2$ polymorph. It is widely recognized that the appropriate anatase to rutile ratio of TiO$_2$ phases is an important parameter to determine the formation of anatase/rutile TiO$_2$ phasejunction [45-48], which are photocatalytically active that could improve the photogenerated charge separation and migration, and suppress the charge recombination [40, 45, 48, 49]. The Rietveld refinements provide further details including estimated particle sizes, volume and density of anatase and rutile phases along with the goodness of fit parameters as shown in Table S1.
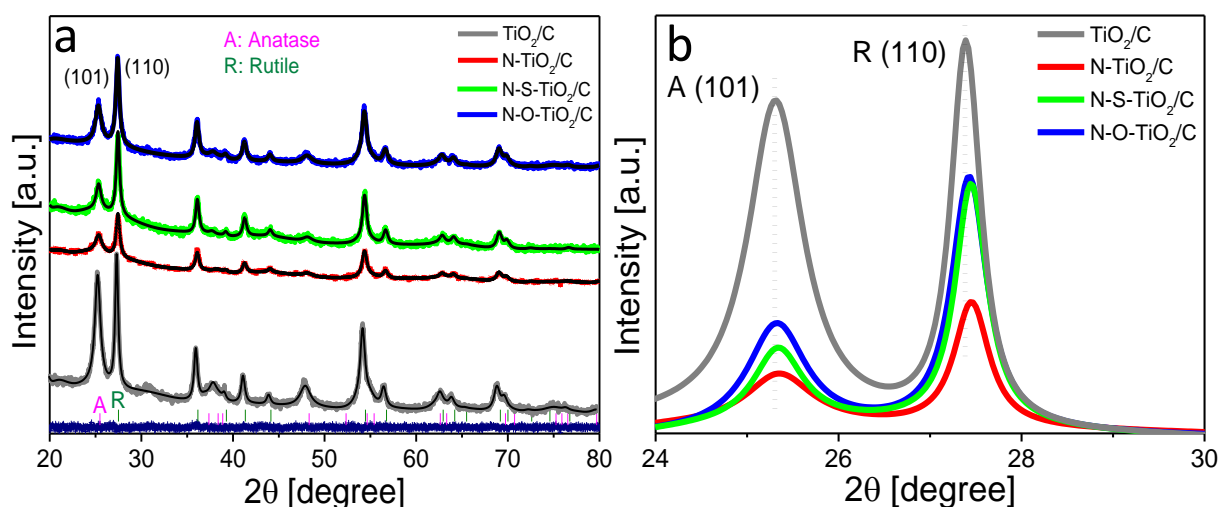
Fig. 1. (a) PXRD patterns with Rietveld refinements and (b) highlighted anatase (101) and rutile (110) peaks of TiO$_2$/C (gray), N-TiO$_2$/C (red), N-S-TiO$_2$/C (green) and N-O-TiO$_2$/C (blue).

As discussed above, during thermal decomposition of Ti-MOFs at higher temperatures in air, the organic linkers in MOFs transform into porous carbon matrix. Thermogravimetric analysis (TGA) profiles of precursors MIL-125(Ti) and NH$_2$-MIL-125(Ti) in the air (Fig. S2) showed a total weight loss of 64.4 and 66.4% respectively due to the removal of residual solvents DMF and MeOH) at above 200 ^{0} C and the release of volatile chemical species like CO$_2$ and NO$_2$ at above 350 ^{0} C, which is due to the breaking of the coordination bonds between organic linker (BDC) and Ti oxo-cluster, as well as the burning off the BDC in air [40, 41]. Differential thermal analysis (DTA) curves of both precursor samples in air also show the breaking of the NH$_2$ functional groups from the organic linker in NH$_2$-MIL-125(Ti) at around 350 ^{0} C and the release of volatile species in the form of NO$_2$ which causes a slightly higher weight loss compared to MIL-125(Ti). The TGA profiles (Fig. S3a) of the Ti-MOFs derived composites TiO$_2$/C, N-TiO$_2$/C, N-S-TiO$_2$/C and N-O-TiO$_2$/C in air show total weight loss of

27.6%, 33.8%, 39% and 28% respectively. The different weight percentage of the released species in these samples indicate the presence of different amount of porous carbon as well as and N, S and O species-based surface functional groups in the pyrolyzed samples. The MS spectra signals (Fig. S3b) of the representative sample N-S-TiO$_2$/C shows that C, N and S species were burned off and released in the form of CO_2, NO_2 and SO_2 along with moisture (H_2O), suggesting the presence of C, N and S species in this composite.

During the pyrolysis of MIL-125(Ti) and NH$_2$-MIL-125(Ti) to derive TiO$_2$/C composites in the controlled atmosphere, it is anticipated that N, S and carboxylate (-OH/-COOH) surface functional groups are produced and attached to the in-situ formed porous carbon matrix. Raman spectra of the obtained sample TiO$_2$/C composite (Fig. 2a) exhibits two signature peaks of D (disorder/defect) and G (graphitic) bands for the in-situ formed porous carbon at 1338 and 1595 cm^{-1} respectively. The D band showed a small Raman shift to 1348 cm^{-1} in samples N-TiO$_2$/C, N-S-TiO$_2$/C and N-O-TiO$_2$/C. Similarly, the G band also showed a significant Raman shift with relatively decreased peak intensities for samples N-TiO$_2$/C and N-S-TiO$_2$/C compared to sample TiO$_2$/C, which indicates that the presence of a higher number of defects in the formed carbons that contain N and S species [36, 50, 51]. The peak intensity ratio of D and G bands (I_D/I_G) represents the number of defects and disorders in crystalline carbon structures. The I_D/I_G ratios were estimated to be 0.92, 1.29, 0.95 and 0.93 for samples TiO$_2$/C, N-TiO$_2$/C, N-S-TiO$_2$/C and N-O-TiO$_2$/C respectively.
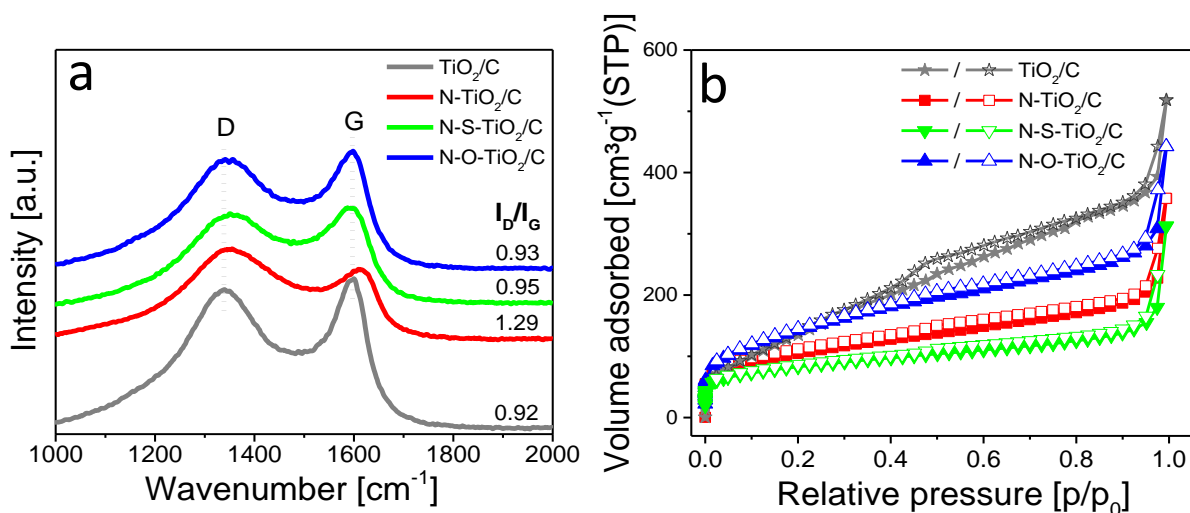
Fig. 2. (a) Raman spectra of TiO_2/C (gray), $N\text{-}TiO_2/C$ (red), $N\text{-}S\text{-}TiO_2/C$ (green) and $N\text{-}O\text{-}TiO_2/C$ (blue) (b). N_2 sorption isotherms of samples TiO_2/C, $N\text{-}TiO_2/C$, $N\text{-}S\text{-}TiO_2/C$ and $N\text{-}O\text{-}TiO_2/C$. The filled and empty symbols represent the adsorption and desorption branch of isotherm respectively.

FTIR spectra (Fig. S4) of the Ti-MOFs derived composites all exhibit a vibrational band at around 3440 cm^{-1} due to the stretching of O-H groups from surface absorbed H_2O. Relatively low intensity but broader peak at around 2000 cm^{-1} (highlighted in the inset) in sample N-S-TiO_2/C can be assigned to the vibrational modes of S species doped into TiO_2 crystal lattice [16]. A smaller peak at 1815 cm^{-1} in sample N-O-TiO_2/C prepared under water vapor atmosphere may appear due to the stretching modes of –COOH functional group in the carbon matrix [40]. Two prominent peaks at around 1620 cm^{-1} and 1385 cm^{-1} in all samples can be assigned to the stretching vibrational modes of C=C in aromatic rings and bending vibrational modes of C-O in the formed carbon matrix respectively. A relatively stronger intensity of the peak with a broader full width half maximum (FWHM) and a slight redshift to 1608 cm^{-1} in sample N-O-TiO_2/C indicates the presence of additional oxygen species (-COOH/-OH) due to the pyrolysis under water vapor atmosphere. A broader peak at around 1130 cm^{-1} with varying intensity in samples TiO_2/C, N-TiO_2/C and N-S-TiO_2/C may indicate the C-N, C-S and/or C-

OH stretching vibrations [52]. A broader band stretched between 1250-1150 cm^{-1} and a smaller peak at 990 cm^{-1} (shown in inset) in sample N-O-TiO$_2$/C can be ascribed to the C-O stretching modes and O-H wagging modes of –COOH functional groups respectively, attached on the porous carbon matrix [34, 40]. The strong vibrational bands between 630 and 620 cm^{-1} in all samples can be attributed to the stretching modes of Ti-O in TiO$_2$ nanoparticles. The relatively lower intensity and appearance of the broader shoulder peak at around 550 cm^{-1} in samples N-TiO$_2$/C, N-S-TiO$_2$/C and N-O-TiO$_2$/C indicate the altered chemical bonding structure of TiO$_2$ due to the different composition of anatase and rutile phases as well as the presence of defects and doped N and/or S species [17]. This observation is in good agreement with the PXRD patterns (Fig. 1). The chemical composition, chemical states and electronic structures of these Ti-MOF derived multi-functionalized and co-doped TiO$_2$/C composites were further investigated by XPS.

The textural properties of MOFs derived composites such as BET surface area and pore size also play important role in photocatalytic performance of the materials. Higher BET surface area with appropriate pore shape/size favors the better adsorption of the photocatalytic reactant species whereas the suitable morphology of composites offers accessible active sites for photocatalytic reactions. The BET surface area and pore size distribution of MIL-125(Ti) and NH$_2$-MIL-125(Ti) derived composites were obtained from N$_2$ sorption isotherms measured at 77 K. As shown in Fig. 2b, all the samples exhibit type IV isotherms with small or negligible hysteresis loops at above the relative pressure (p/p$_0$) of 0.4. The adsorption below p/p$_0$ of 0.1 confirms the formation of micropores. A small hysteresis loop at p/p$_0$ above 0.4 in samples N-TiO$_2$/C, N-S-TiO$_2$/C and N-O-TiO$_2$/C is due to the capillary condensation in mesopores. However, the sample TiO$_2$/C shows relatively larger hysteresis loop between relative pressure p/p$_0$ 0.4 and 0.9 which suggests the predominance of the mesopores. The BET specific surface areas were calculated to be 558, 373, 282 and 513 m^2 g^{-1} for samples TiO$_2$/C, N-TiO$_2$/C, N-S-

TiO$_2$/C and N-O-TiO$_2$/C respectively. Compared to the other samples, the relatively lower BET surface area of sample N-TiO$_2$/C and N-S-TiO$_2$/C might be due to the formation of a minimal amount of TiN and TiS$_2$ (along with TiO$_2$ nanoparticles) during the pyrolysis of NH$_2$-MIL-125(Ti) under argon and H$_2$S gaseous atmosphere which may block the pores, making them inaccessible for the adsorption of N$_2$ molecules. The NLDFT pore size distribution (PSD) (shown in Fig. S5) of N-TiO$_2$/C, N-S-TiO$_2$/C and N-O-TiO$_2$/C exclusively exhibit pore widths at around 1.4 nm and a small amount of mesopores with size of 2.8 nm. The sample TiO$_2$/C obtained from MIL-125(Ti) predominantly possesses mesopores with sizes ranging from 2.5 nm to 4 nm, accompanied with a small amount of micropores centered at around 1.7 nm. Moreover, sample TiO$_2$/C possesses higher pore volume than the other 3 composite samples. Table S2 presents a summary of the BET surface areas, pore sizes and pore volumes of the studied samples.

XPS elemental surveys of the derived composites TiO$_2$/C, N-TiO$_2$/C, N-S-TiO$_2$/C and N-O-TiO$_2$/C are shown in Fig. 3a, which confirm the presence of Ti, O, C and N or S species in relevant samples. The high-resolution scans of Ti 2p (Fig. 3b) show Ti 2p$_{3/2}$ and Ti 2p$_{1/2}$ core level peaks centered at around 459 and 464.7 eV respectively with a doublet splitting $\Delta E_{B.E}$ = 5.7 eV, confirming the presence of Ti^{4+} oxidation state in TiO$_2$. In sample TiO$_2$/C, Ti 2p$_{3/2}$ peak appeared at 459.2 eV. However, this peak was slightly shifted to lower binding energy of 458.9 eV in sample N-TiO$_2$/C which might be caused by the presence of N doped species and oxygen-related defects in TiO$_2$ crystal lattice. A deconvoluted small shoulder-like peak in N-TiO$_2$/C sample can be assigned to Ti-N chemical bonds [53]. In samples N-S-TiO$_2$/C and N-O-TiO$_2$/C, Ti 2p$_{3/2}$ peak appeared at 459.06 and 459.02 eV respectively along with the deconvoluted low-intensity shoulder peaks for Ti-N chemical bonds. This small shift in binding energy confirms the presence of N, S and oxygen-rich doped species perturbing the local chemical environment of TiO$_2$ [12, 40].
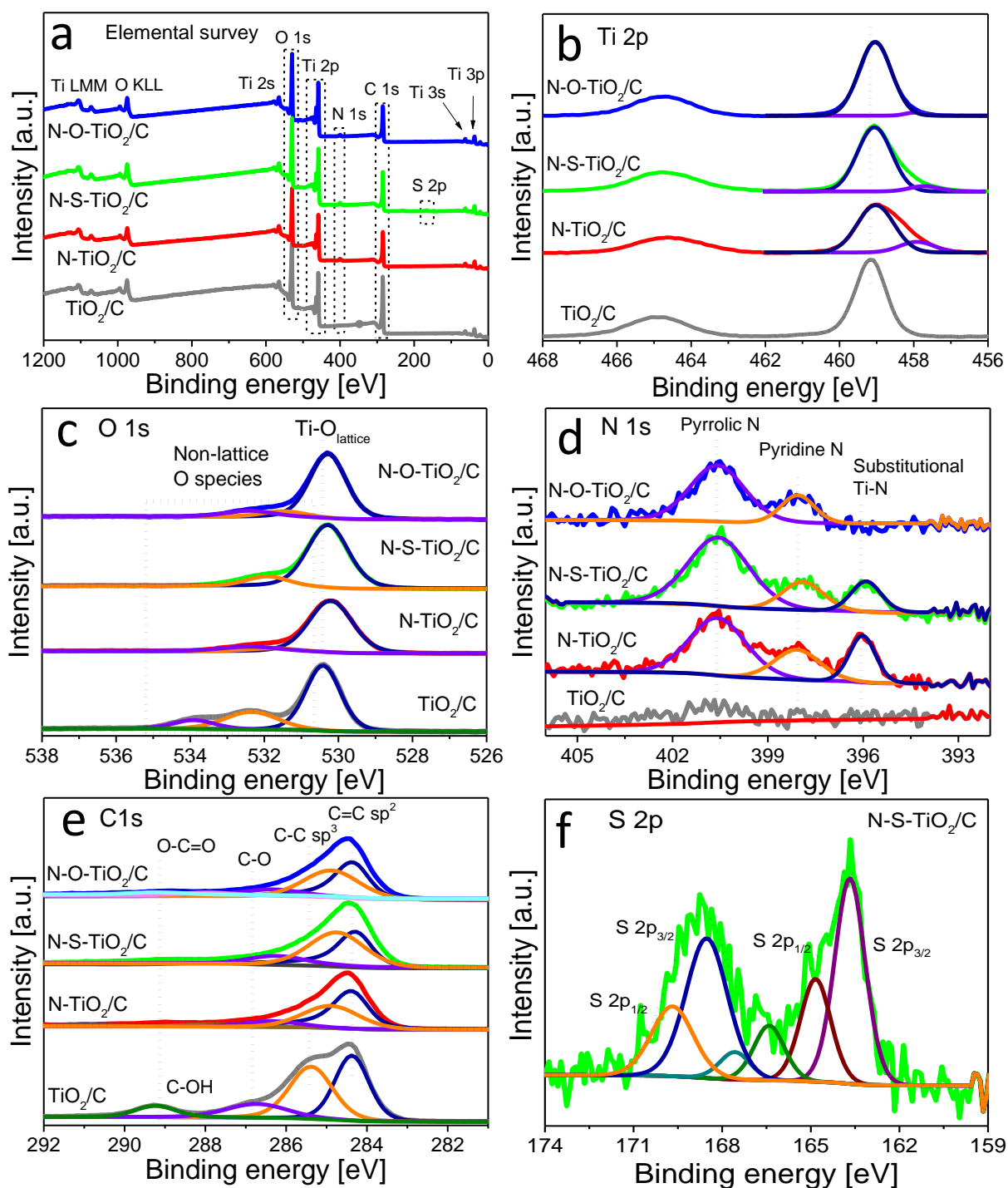
Fig. 3. XPS spectra of (a) elemental survey (b) Ti 2p (c) O 1s (d) N 1s (e) C 1s and (f) S 2p of samples TiO$_2$/C, N-TiO$_2$/C N-S-TiO$_2$/C and N-O-TiO$_2$/C.

The deconvoluted O 1s spectra (Fig. 3c) of TiO_2/C sample exhibited the main peak at 530.41 eV which is a signature peak of Ti-O in TiO_2 crystal lattice. In sample N-TiO_2/C, this peak appeared at 530.21 eV, whereas it slightly shifted to 530.28 eV in samples N-S-TiO_2/C and N-O-TiO_2/C. The shifting of Ti-O peaks to lower binding energies confirms the formation of oxygen-related defects and vacancies due to the N and S species doped during the pyrolysis of MOF precursors. The second deconvoluted peak of O 1s (orange colored line) appeared at around 532.3, 531.7, 531.9 and 531.5 eV in samples TiO_2/C, N-TiO_2/C, N-S-TiO_2/C and N-O-TiO_2/C respectively, can be ascribed to the -OH groups present on the surface of the composites. These -OH species are produced from the breaking of coordination bonds between Ti oxo-cluster and organic linkers as well as the decomposition of $C_6H_4(COOH)_2$ (BDC) or NH_2-BDC. In sample N-O-TiO_2/C, an additional small peak appeared at 532.39 eV (violet line) which can be attributed to the O=C-O functional groups attached on the surface of porous carbon matrix due to the pyrolysis of NH_2-MIL-125(Ti) under the water vapor gaseous atmosphere [34]. An additional smaller peak appeared at 533.9 eV in sample TiO_2/C can be assigned to the other non-lattice O species including and oxygen related defects and vacancies.[54]

The XPS spectra of N 1s (Fig. 3d) shows that no N 1s peak was observed in sample TiO_2/C. However, two peaks appearing at around 400.60 and 398.08 eV in samples N-TiO_2/C, N-S-TiO_2/C and N-O-TiO_2/C can be assigned to the pyrrolic N and pyridine N species present on porous carbon matrix [17, 50]. It is interesting to note that samples N-TiO_2/C and N-S-TiO_2/C exhibited third peak at 396.02 and 395.91 eV respectively, which can be attributed to the substitutional N atoms forming Ti-N bonds in TiO_2 crystal lattice [17, 53]. However, this peak is completely absent in sample N-O-TiO_2/C. During the high temperature pyrolysis of NH_2-MIL-125(Ti) under argon, N species from $-NH_2$ functional groups could replace O 2p states with N1s states to form substitutional Ti-N bonds, causing the N doping into TiO_2 lattice.

When NH_2-MIL-125(Ti) was pyrolyzed in argon and H_2S gaseous atmosphere to prepare composite N-S-TiO$_2$/C, both the N atoms and the S atoms can replace O 1s through S→O exchange which further modifies the electronic structure of TiO$_2$. It is worth noting that the ionic radius of S^{2-} is larger than that of O^{2-}, therefore, the relatively small amount of doped S species along with the N species favor the formation of additional defects in TiO$_2$ crystal lattice [16]. However, the absence of the substitutional N 1s peak in sample N-O-TiO$_2$/C indicates that under water vapor atmosphere, the presence of an excess amount of oxygen species suppresses the formation of substitutional Ti-N species; instead, oxygen-rich N-O like interstitial/intraband (Ti- O-N) states can be formed [40, 53]. It is assumed that under water vapor atmosphere, oxygen species compete with and dominate N atoms doping into TiO$_2$, which results in preventing the substitution of the O 2p by N 1s in TiO$_2$. It is well understood that the formation of doping states via non-metal dopants introduces additional electronic levels above the valance bands, which narrows the energy band gaps [10, 53, 55]. This was further confirmed by XPS valence band edge spectra.

The XPS peaks of core level C 1s (Fig. 3e) appeared at 284.37, 285.38 and 286.72, 289.23 and 290.75 eV in sample TiO$_2$/C correspond to C=C sp^2 aromatic bonding, C-C sp^3 bonding and C-O bonds, C-OH bonds from the decomposition of organic linker and π-π* bonds respectively [50, 56, 57]. The shift in binding energy peak positions along with the varied FWHM and intensities of core level C 1s in samples N-TiO$_2$/C, N-S-TiO$_2$/C and N-O-TiO$_2$/C clearly indicate the formation of different surface defects and presence of functional groups on porous carbon. It suggests the importance of the gaseous atmosphere in the pyrolysis of MOFs. Compared to sample TiO$_2$/C, the C-C sp^3 binding energy peak in samples N-TiO$_2$/C and N-O-TiO$_2$/C appeared to 284.9 eV which clearly signifies the formation of defects in graphitic carbon due to the presence of N functional groups. The increase in the intensity of this peak with a small shift to 284.7 eV in sample N-S-TiO$_2$/C indicates the further growth of surface

defects due to the presence of S functional groups on porous carbon. Moreover, compared to sample TiO_2/C, a decrease in the intensity of the C-O peak with a slight shift toward lower binding energy in samples $N-TiO_2/C$, $N-O-TiO_2/C$ and $N-S-TiO_2/C$, appearing at 286.35, 286.34 and 286.26 eV respectively, may also suggest the replacement of O species with N and S species and the formation of C-N and C-S bonds respective. In sample $N-O-TiO_2/C$, an additional peak observed at 289.09 eV represents the carboxylate (O-C=O) functional groups formed on the surface of porous carbon due to the pyrolysis of NH_2-MIL-125(Ti) under water vapor atmosphere [34, 40]. The surface attached -OH/-COOH functional groups may also contribute to the improvement of the hydrophilicity of these derived composites.

The core level S 2p XPS spectra (Fig. 3f) of $N-S-TiO_2/C$ are deconvoluted into S $2p_{3/2}$ and S $2p_{1/2}$ peaks appeared at 168.56 and 169.76 eV respectively, from Ti-S, which is formed during high temperature pyrolysis as the O^{2-} is exchanged by the S^{2-} species co-doping the TiO_2 crystal lattice [58]. The two deconvoluted peaks with relatively lower intensity, appeared at 167.56 and 166.4 eV, can be assigned to the sulfoxide and sulfones ($-SO_2-C$) groups attached to the amorphous carbon matrix [59]. The other prominent S 2p peaks of S $2p_{3/2}$ and S $2p_{1/2}$ at 163.66 and 164.84 eV respectively, correspond to covalent bonded C-S-C species in N doped carbon matrix respectively [57, 60]. Based on the XPS measurements, a summary of atomic concentrations of Ti 2p, O 1s, N 1s, S 2p and C 1s in these MOF derived composites was presented in Table S3.

3.2. Morphology and optical properties

Scanning electron microscope (SEM) and transmission electron microscope (TEM) images of the precursor NH_2-MIL-125(Ti) (Fig. S6a and b) show the tetragonal 3D disc-like morphology (SEM) with well crystalline structure (TEM). During the pyrolysis of the precursors at 800 ^{0} C under the relevant gaseous atmosphere, the coordination bonds between

Ti oxo-cluster and organic linkers break and Ti oxo-clusters transform into N and/or S self-doped TiO_2 nanoparticles and the organic linkers (BDC or NH_2-BDC) convert to a surface-functionalized amorphous porous carbon matrix. The particle sizes exhibit a volumetric shrinkage of around 35 % but the shape/morphology of the crystallites remain unchanged [42]. Fig. S7 confirms the preservation of the 3D disc-like tetragonal morphologies of the sacrificial templates in the derived resulting TiO_2/C composites. The slight difference of morphology of sample N-O-TiO_2/C with less small particles on the surface compared to other samples is possibly due to its pyrolysis in water vapor at high temperature. The presence of oxygen-rich water vapor may enable the Ti species from the framework of MIL-125 more easily react with oxygen to form TiO_2 species and aggregate to form relative larger particles. The TEM images of the derived composites (Fig. S8) show that due to the shrinkage of porous carbon matrix at a high pyrolysis temperature of 800 ^{0} C, some TiO_2 nanoparticles are exposed on the surface of the derived composites. Moreover, it also confirms the uniform distribution of TiO_2 nanoparticles with particle sizes around 10 nm for anatase phase and 20 nm for rutile phase, which are in very good agreement with the particle sizes distribution calculated from Rietveld refinement (Table S1). The high-resolution TEM images of the derived composites (Fig. 4a-d) show an obvious change in crystal lattice spacing of N and/or S doped TiO_2 nanoparticles. The lattice spacing of rutile TiO_2 (110) was estimated to be 0.33, 0.337, 0.34 and 0.322 nm for samples TiO_2/C, N-TiO_2/C, N-S-TiO_2/C and N-O-TiO_2/C respectively. The varying values of TiO_2 lattice spacing in these composites are due to the presence of dopants like N and/or S species, the defects and oxygen vacancies.
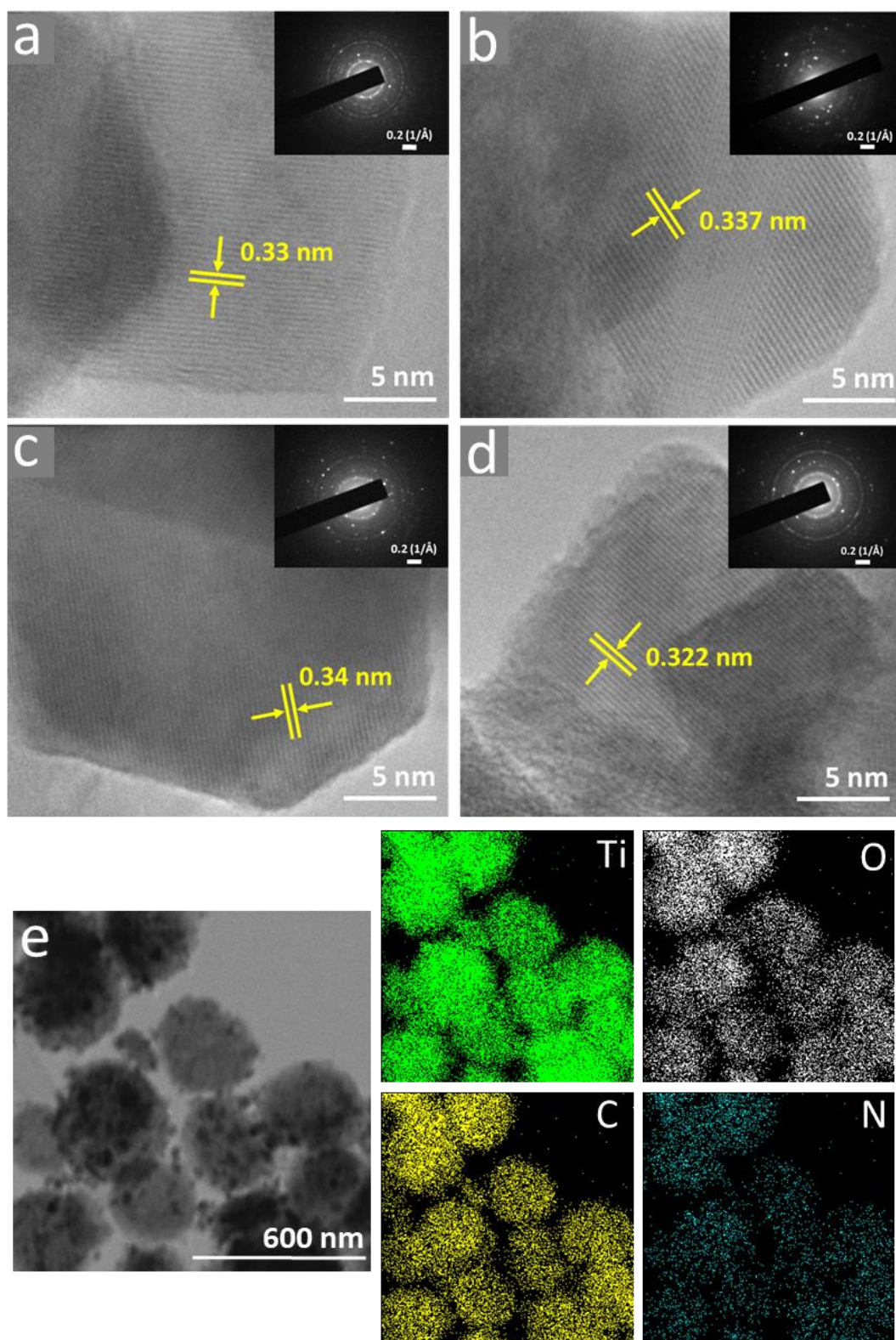
Fig. 4. HRTEM images of (a) TiO$_2$/C (b) N-TiO$_2$/C (c) N-S-TiO$_2$/C and (d) N-O-TiO$_2$/C. Inset images show the selected area electron diffraction (SAED) patterns of the respective samples. (e) EDX elemental mappings of Ti, O, C and N of a selected sample N-O-TiO$_2$/C.

22

EDX elemental mappings of the derived composites (Fig. 4e and S9) confirm that the formed TiO_2 nanoparticles are immobilized and uniformly distributed throughout the carbon matrix without agglomeration due to the barriers provided by the amorphous carbon. However, as demonstrated by the gas sorption analysis, the pore sizes of the derived composites turn to larger compared to the MOFs precursors. The uniform distribution of TiO_2 nanoparticles in porous carbon matrix makes them well exposed to the incident light as well as adsorbed organic pollutant species. The easily accessible active sites can significantly improve the overall photocatalytic activity of the composites.

The optical property of a semiconducting material primarily depends on its energy band gap that reflects the capability of electrons migration from the occupied valance band to the unoccupied conduction band [61, 62]. The energy band gaps of pure anatase and rutile TiO_2 nanoparticles are usually observed at 3.2 and 3.0 eV respectively. When the dopants, defects and impurities including metal and non-metal elements are introduced into the crystal lattice, additional electronic states/levels can be formed below the conduction band or above the valence band respectively. In the case of TiO_2, the valence band edge comprises of O 2p orbitals and conduction band edge of Ti 3d orbitals [62]. The introduce of non-metal dopants including N and S atoms could form interstitial states above the valence band edge or replace the O 2p atoms to form substitutional Ti-N and Ti-S bonding states [55, 63]. As a result, the N and S doping into TiO_2 may introduce additional electronic transition states with increased density of states that narrows the energy band gap, resulting in inferior TiO_2 photoactive under the visible light [62]. The XPS valence band spectra (Fig. 5a) show that the valence band edge in sample TiO_2/C was at 3.10 eV, whereas the valence band edge shifted towards lower binding energy of 2.78 and 2.64 eV in samples N-TiO_2/C and N-S-TiO_2/C, respectively. It clearly suggests that the doped N and S species have partially substituted the oxygen species in TiO_2 nanocrystals, which results in the produce of defects and oxygen vacancies, as well as the formation of

additional electronic states above the valence band that shifts the valence band edge and consequently narrows the energy band gap. However, in sample N-O-TiO$_2$/C which was prepared under water vapor gaseous atmosphere, the presence of excessive oxygen species prevents the N atoms to replace oxygen species in valence band, as a result, oxygen-rich N-O like interstitial/intraband with localized N 2p states are formed close to the valence band [40, 53, 61, 63]. Due to the absence of substitutional N species in sample N-O-TiO$_2$/C which was also confirmed by XPS N 1s spectra in Fig. 3d, the valence band edge of N-O-TiO$_2$/C sample showed a negligible shift in binding energy (2.79 eV) compared to the sample N-TiO$_2$/C. Instead, the interstitial/intraband oxygen-rich N-O species like dopants may give rise to the π bonding states below the O 2p band and the occupied π^* anti-bonding states above the O 2p band [53, 64]. It was reported that such localized occupied states might be difficult to distinguish by XPS valence band edge of O 2p band, especially in multi-species co-doped complex composites. Nevertheless, they contribute to the visible-light-induced photocatalytic activity of the photocatalyst [53, 64]. Moreover, compared to the sample TiO$_2$/C, the observed changes in the position, slope and intensity of the valence band spectra in Fig. 5a also confirm the presence of additional density of states above the valence bands of samples N-TiO$_2$/C, N-S-TiO$_2$/C and N-O-TiO$_2$/C [65]. In addition, the UV-Vis absorption spectra (Fig. 5b) of pure TiO$_2$ show an absorption band edge at < 390 nm, but sample TiO$_2$/C, N-TiO$_2$/C, N-S-TiO$_2$/C and N-O-TiO$_2$/C showed a redshift in their absorption band edge to 464, 472, 477 and 482 nm respectively [62, 66]. It is worth noting that along with the N and/or S doping, the presence of carbon species and the growth of rutile phase of TiO$_2$ with respect to the anatase phase in samples N-TiO$_2$/C and N-S-TiO$_2$/C also influence the narrowing of the overall energy band gap of the composites.
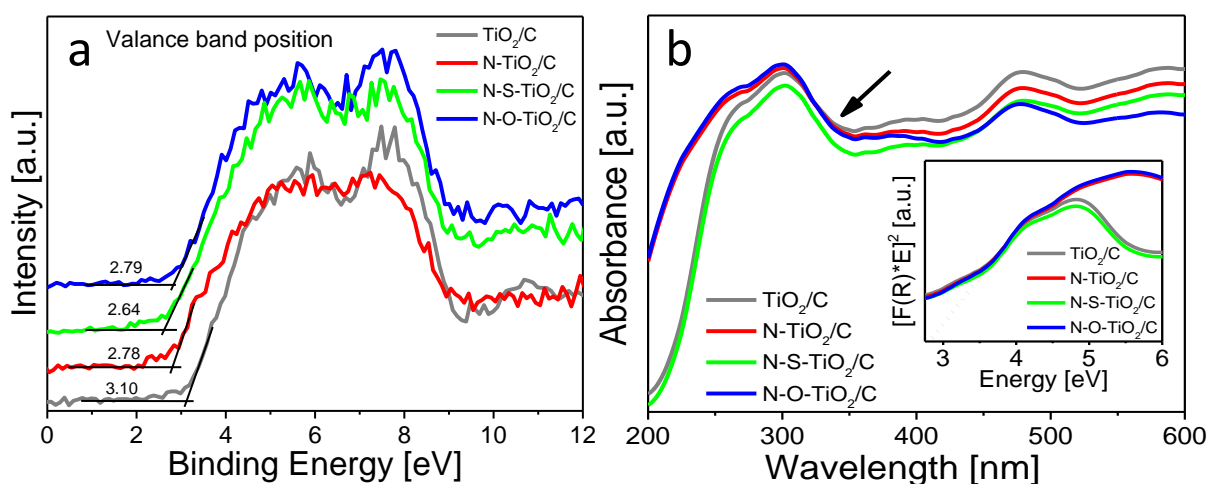
Fig. 5. (a) XPS valance band edge spectra and (b) UV-Vis absorption spectra of samples TiO$_2$/C, N-TiO$_2$/C, N-S-TiO$_2$/C and N-O-TiO$_2$/C. Inset in b shows the Tauc plots of the samples.

3.3. Photodegradation performance and photocatalytic mechanism

The degradation and photocatalytic performance of MIL-125(Ti) and NH$_2$-MIL-125(Ti) derived composites was tested in dark and under visible light. The kinetics of adsorption of MB by the different nanocomposites were evaluated by applying various kinetic models. As shown in Fig. 6a, no self-degradation of methylene blue (MB) was observed in dark. As a comparison, the commercially available TiO$_2$ (P-25) was used as a reference sample and it showed only 0.7% adsorption in dark due to its non-porous nature. The Ti-MOFs derived composite samples TiO$_2$/C, N-TiO$_2$/C, N-S-TiO$_2$/C and N-O-TiO$_2$/C exhibited 57, 26, 28 and 32% adsorption of MB after 180 minutes in dark respectively. The adsorption by all the composite samples mainly took place in the first 30 minutes. Actually, the predominated adsorption of MB happens in the first 10 minutes for samples TiO$_2$/C, N-TiO$_2$/C and N-O-TiO$_2$/C, followed by an almost flat curve, implying the achieving of adsorption/desorption equilibrium (Fig. 6a). The higher percentage of MB adsorption by composite TiO$_2$/C in dark is

due to its relatively higher surface area (558 $m^2 g^{-1}$) and the presence of larger pores (mesopores with sizes > 2 nm).

To illustrate the effect of surface functionalization and textural properties on the adsorption of MB, four kinetic models including pseudo first-order, pseudo second-order, Elovich kinetic and intraparticle diffusion models (Fig. 6b-e) were applied to calculate the rate of adsorption reaction and rate-controlling factors in the MIL-125(Ti) and NH_2-MIL-125(Ti) derived composites [9, 67]. The values of the relevant parameters of the four kinetic models for samples TiO_2/C, N-TiO_2/C, N-S-TiO_2/C and N-O-TiO_2/C are summarized in Table S4. Among the four fitted models, pseudo second-order kinetic model exhibits the highest values of correlation coefficient of $R^2 = 0.99$ for the adsorption of MB by composite samples TiO_2/C, N-TiO_2/C, N-S-TiO_2/C and N-O-TiO_2/C, indicating it is the best fittings of the model. Therefore, pseudo second-order kinetic model is the best to describe the kinetics of adsorption and degradation of MB by these studied MOF-derived composites. The pseudo second-order rate reaction depends upon the amount of the solute adsorbed on the surface of the catalyst (adsorbent) and the amount being adsorbed at equilibrium [68]. According to this model, the composite TiO_2/C showed the highest equilibrium adsorption capacity (q_e) of 59.77 mg·g^{-1} compared to other composites, which exhibited maximum equilibrium adsorption capacities of 26.49, 29.39 and 31.74 mg·g^{-1} for samples N-TiO_2/C, N-S-TiO_2/C and N-O-TiO_2/C, respectively. The higher equilibrium adsorption capacity of MB by TiO_2/C can be attributed to the relatively larger surface area, predominant mesopores and higher pore volume. Clearly, the best fitted R^2 values of the pseudo second-order model in these composite samples suggests that the higher BET surface area and the surface-attached hydroxyl /carboxylate (-OH/-COOH) functional groups play the key role in facilitating faster adsorption of MB molecules and access to the active sites [67, 68]. The intraparticle diffusion model exhibits linear plot of $t^{1/2}$ verses q_t if the intraparticle diffusion is involved as a rate-controlling factor only [67, 69]. In this

model, two or more slopes could also occur in case of the multistep adsorption process. As shown in Fig. 6e, rapid adsorption of MB on composites TiO_2/C, $N-TiO_2/C$ and $N-O-TiO_2/C$ in first 30 minutes occurred due to the boundary layer diffusion which can be attributed to the predominant mesopores and the slow adsorption in the following 2.5 hours (intraparticle diffusion indicated by the second slope in Fig. 6e) could be due to the presence of micropores [70]. In general, the intraparticle diffusion model exhibits the lowest values of correlation coefficient of R^2, suggesting this model is not appropriate for the adsorption of MB on those studied composite materials. Both, pseudo first-order equation and Elovich equation give intermediate values of correlation coefficient of R^2 and Elovich equation kinetic model generally produce higher R^2 values than pseudo first-order equation model.
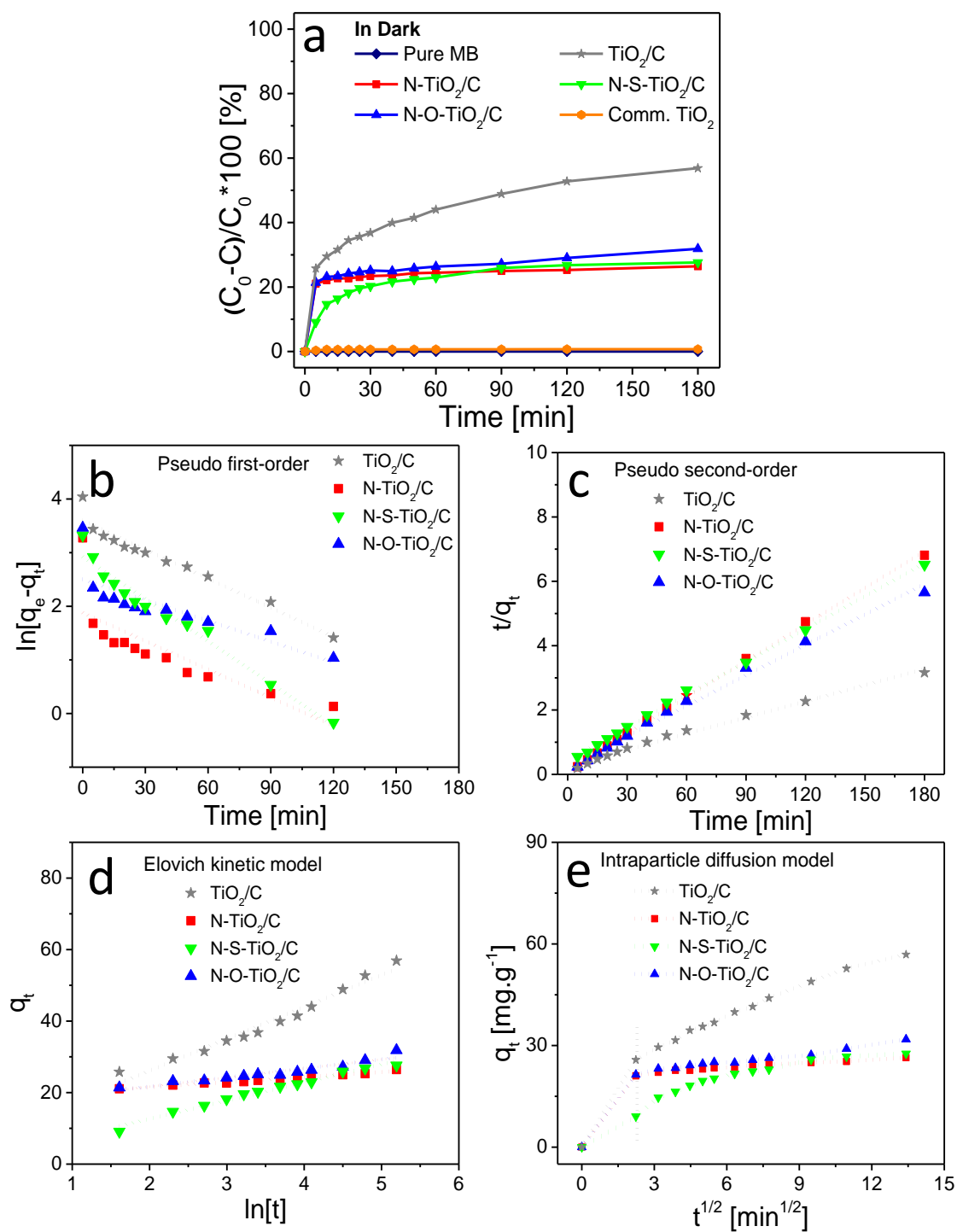
Fig. 6. (a) Adsorption of MB in dark for samples TiO$_2$/C (gray star), N-TiO$_2$/C (red square), N-S-TiO$_2$/C (green downward triangle), N-O-TiO$_2$/C (blue upward triangle), pure MB (navy blue tetragonal) and comm. TiO$_2$ (orange hexagonal). Fitting with (b) pseudo first-order, (c) pseudo second-order, (d) Elovich kinetic model and (e) intraparticle diffusion model for the

28

studied composite samples TiO_2/C, N-TiO_2/C, N-S-TiO_2/C and N-O-TiO_2/C. (The adsorption measurement conditions: MB concentration: 20 mg L^{-1}, catalyst dosage: 200 mg L^{-1}, and measured at room temperature)

Under the irradiation of visible light, the UV-Vis absorption spectra of photodegradation of MB by a representative composite sample N-O-TiO_2/C was recorded after certain time intervals (Fig. S10). Obviously, complete mineralization of MB with no new peaks of secondary pollutants was observed. As shown in Fig. 7a, under the irradiation of visible light, the nanocomposite samples TiO_2/C, N-TiO_2/C, N-S-TiO_2/C and N-O-TiO_2/C demonstrated overall 70, 52, 57 and 99.7% photodegradation activity of MB in 3 hours respectively. It is worth noting that under the irradiation of visible light, the adsorption and photocatalytic dye degradation take place simultaneously. Although it is difficult to distinguish the contribution of adsorption from photodegradation of MB, it is however clear that after 3 hours of visible light exposure, sample TiO_2/C demonstrated an additional 17% of photodegradation activity compared to its performance in the dark condition; Moreover, after exposure to visible light for 3 hours, samples N-TiO_2/C and N-S-TiO_2/C also exhibited 26% and 29% higher photodegradation activity of MB than their performance in the dark respectively. Interestingly, composite N-O-TiO_2/C displayed the best photodegradation activity of 99.7% under the visible light in 3 hours, which is 68% improvement compared to its activity in dark condition, implying the completely removal of MB from the water solution under visible light for composite N-O-TiO_2/C. Actually, compared with the TiO_2/C nanocomposites reported for the photodegradation of organic pollutants in the literature (Table S5), sample N-O-TiO_2/C demonstrates to be one of the most efficient photocatalyst to decompose MB under visible light.

In Ti-MOFs derived TiO_2/C composites, the chemical compositions, the crystalline structures with appropriate ratio of anatase/rutile phases in TiO_2 phasejunction, the textural

properties including higher surface area and suitable pore sizes, the optical properties with narrow energy band gap through doping as well as the surface properties synergistically contribute to the photocatalytic activity of those samples. The composite $N-TiO_2/C$ demonstrates considerably improved photocatalytic activity compared to the sample TiO_2/C due to the presence of N species on the surface of porous carbon matrix as well as the doped N into the TiO_2 nanoparticles, as confirmed by PXRD, FTIR, Raman and XPS spectra. Introducing of sulfur species via H_2S gaseous atmosphere as additional functional groups such as sulfoxide and sulfone (confirmed by FTIR and XPS, S 2p) on porous carbon matrix and S co-dopant into TiO_2 to form Ti-S bond in the composite $N-S-TiO_2/C$ helped to double the photodegradation activity of MB from 28% in dark to 57% in visible light, due to the formation of additional localized states above valence band which further narrows the energy band gap (Fig. 5a). However, amongst all the studied composites, sample $N-O-TiO_2/C$ which was obtained from the pyrolysis of NH_2-MIL-125(Ti) under water vapor atmosphere, exhibits the highest improvement in photodegradation activity of MB in visible light compared to in dark, likely due to the presence of carboxylate functional groups (-COOH) on the surface of the porous carbon matrix in the composite and oxygen-rich intraband N-O like localized interstitial states in TiO_2. These surface-attached -OH/-COOH functional groups increase the hydrophilicity of the composite and provide additional photocatalyic active sites which facilitate the MB molecules to be better accommodated on the surface and inside the pores, resulting in a superior adsorption and photodegradation performance of this composite sample.
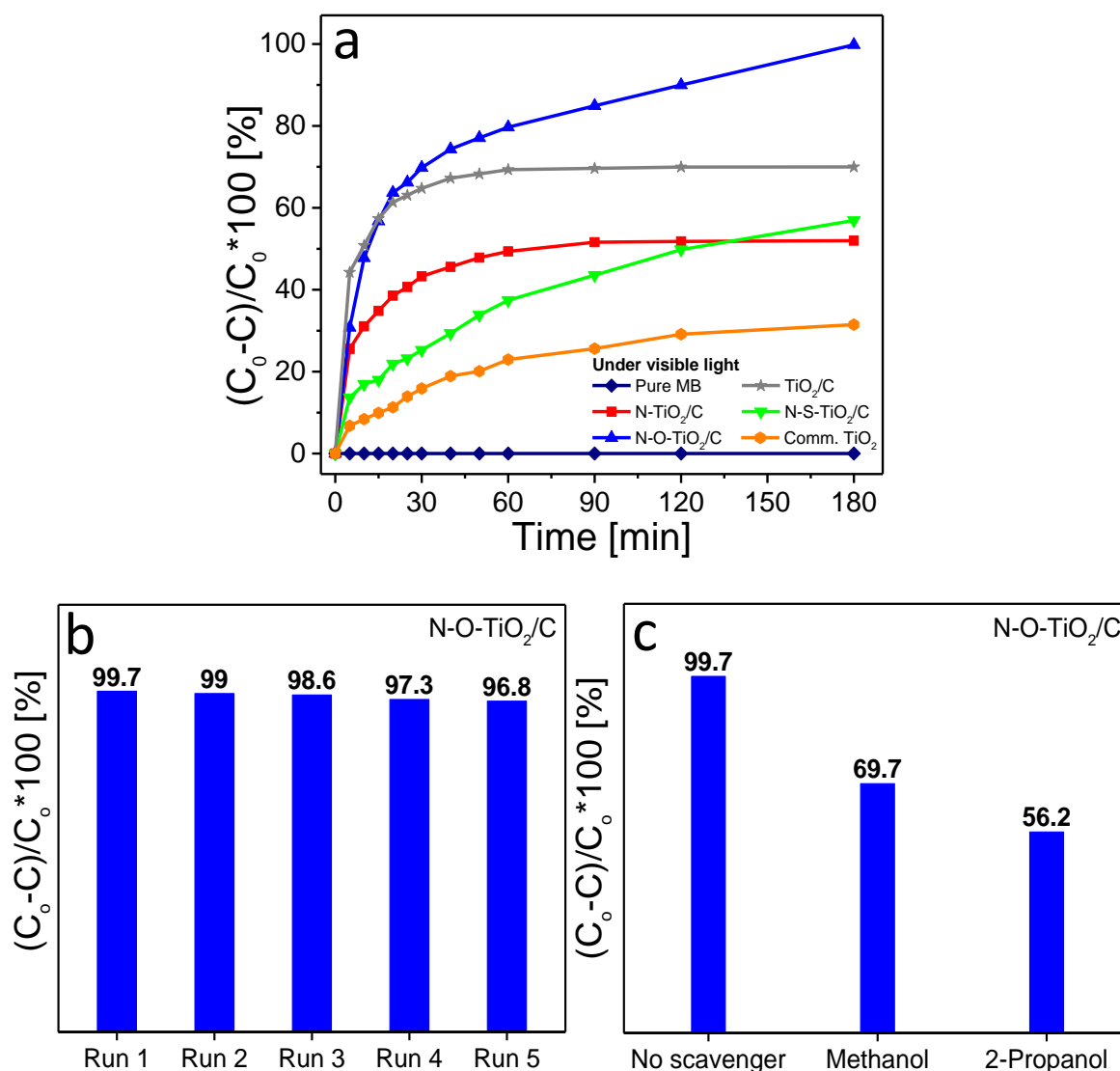
Fig. 7. Photodegradation of MB under (a) visible light conditions for samples TiO$_2$/C, N-TiO$_2$/C, N-S-TiO$_2$/C, N-O-TiO$_2$/C, only pure MB and Comm. TiO$_2$; (b) Recyclability test of the best-performed sample N-O-TiO$_2$/C and (c) the active species trapping experiment quantify the contribution of the photogenerated holes (h$^+$) and hydroxyl radicals ($^\cdot$OH) in photocatalytic oxidation reactions. (The measurement conditions: MB concentration: 20 mg L^{-1}; catalyst dosage: 200 mg L^{-1}; Light source: 380 < λ < 700 nm.)

To determine the hydrophilic and hydrophobic nature of the composites, the water contact angles of these studied samples (Fig. S11) were measured by the sessile drop method [71]. After 0.3 seconds of releasing the water droplet onto the surface of the composite, the water contact angles were optically measured to be 9.5^0 , 15^0 , 8.5^0 and 5^0 for samples TiO_2/C, $N\text{-}TiO_2/C$, $N\text{-}S\text{-}TiO_2/C$ and $N\text{-}O\text{-}TiO_2/C$ respectively, which validates the excellent hydrophilic nature or super wettability of the composites. In particular, $N\text{-}O\text{-}TiO_2/C$ composite functionalized with carboxylate (-COOH) groups demonstrated superhydrophilicity which is in good agreement with the adsorption and photodegradation performance results.

To investigate the stability and reusability of the studied photocatalytic composites, recyclability tests were carried out. The best-performed sample $N\text{-}O\text{-}TiO_2/C$ was evaluated for 5 consecutive MB photodegradation cycles under the visible light. After each photodegradation test, the used photocatalyst was filtered from the solution and washed with deionized water several times followed by drying at 110^0 C overnight. The dried catalyst was reused for the next run without any additional treatment. After 5 consecutive runs (Fig. 7b), the $N\text{-}O\text{-}TiO_2/C$ showed a negligible decrease of photodegradation efficiency, signifying very good physical and mechanical stability of the composite in photodegradation of MB under the irradiation of visible light.

To understand the photocatalytic mechanism of $NH_2\text{-}MIL\text{-}125(Ti)$ derived $N\text{-}O\text{-}TiO_2/C$ composite, active species trapping experiment was performed to determine the primary active oxidative/reductive species contributing to the photodegradation of MB under visible light. Methanol (MeOH) and 2-propanol (IPA) were used as hole (h^+) scavenger and hydroxyl radical (•OH) scavenger respectively [22]. After 3 hours of visible light irradiation (Fig. 7c), the MeOH (h^+ scavenger) inhibited 30% of photodegradation of MB, whereas the 2-propanol (•OH radical scavenger) suppressed more than 43% of photodegradation of MB. These experiments confirm that during the photodegradation of MB, both h^+ and •OH radical are important intermediate

species which take part in and affect the photodegradation performance of MB. Actually, the photodegradation of MB might have taken place due to the reduction reaction caused by the superoxide radical anions ($O_2^{\bullet-}$). A potential schematic diagram of photocatalytic degradation of MB under visible light by a representative Ti-MOFs derived N-O-TiO_2/C composite is proposed in Fig. 8. When visible light is irradiated on Ti-MOF derived N-O-TiO_2/C composites, the holes (h^+) and electrons (e^-) are generated in valence and conduction bands of TiO_2 respectively. Due to the presence of anatase/rutile phasejunction, the e^- from the conduction band of the rutile TiO_2 migrate to the conduction band of anatase TiO_2, whereas the h^+ from the valance band of anatase TiO_2 transfer to the valence band of TiO_2 due to the alignment of their energy band positions [40, 46, 72]. The oxidation reactions take place at valence band of rutile TiO_2 whereas the reduction reactions are carried out at the conduction band of anatase TiO_2. These TiO_2 nanoparticles are uniformly distributed in -N/-COOH functionalized carbon matrix, the photogenerated charges can also migrate to the porous carbon matrix which offers additional photocatalytic active sites. Moreover, the hydrophilic functional groups on the high surface area porous carbon enhance the adsorption of MB and facilitate the interaction between TiO_2 and water molecules, which significantly improves the photocatalytic activities [34, 36, 68]. The photogenerated holes (h^+) react with water molecules to produce •OH radicals. The h^+ can also directly contribute to the oxidation reaction to mineralize MB. On the other hand, the photogenerated electrons (e^-) from the conduction band of TiO_2 or the surface of porous carbon react with oxygen species in water to produce superoxide radical anions ($O_2^{\bullet-}$) which cause the reduction reaction, consequently mineralizing the MB molecules into H_2O and CO_2 [12, 22, 34, 73].
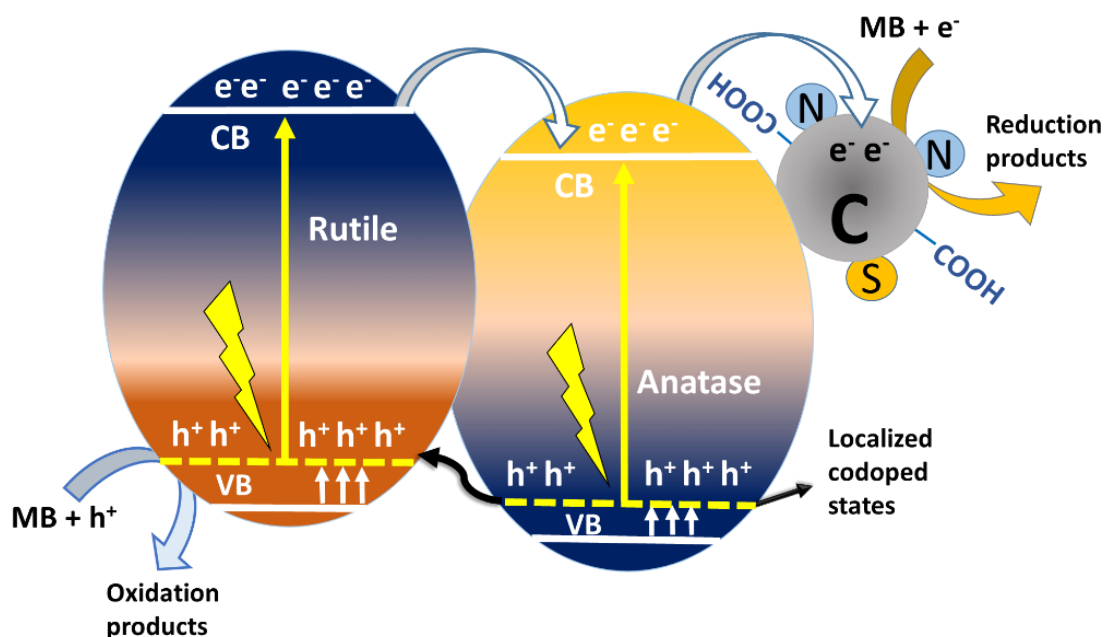
Fig. 8. A proposed schematic diagram of the photocatalytic degradation of MB by Ti-MOF derived composites.

4. Conclusions

Multi-functionalized co-doped TiO_2/C nanocomposite materials derived from the pyrolysis of Ti-MOFs such as MIL-125(Ti) and NH_2-MIL-125(Ti) at 800 ^{0}C in different gaseous atmospheres including argon, water vapor and H_2S were produced, and their photocatalytic performance of MB degradation were evaluated. These Ti-MOFs derived composites TiO_2/C, N-TiO_2/C, N-S-TiO_2/C and N-O-TiO_2/C possess homogeneously distributed TiO_2 nanoparticles in a 3D disc-like porous carbon matrix, and they exhibited 70, 52, 57 and 99.7% photodegradation activity of MB in 3 hours under visible light respectively, compared to only 30% photodegradation of MB for commercial TiO_2 under the same conditions. Based on the detailed characterizations and photodegradation application results, it can be concluded that the gaseous atmosphere during pyrolysis plays a critical role in surface functionalization and doping of the composites. The adsorption and degradation of methylene

blue (MB) in dark on these TiO_2/C composites are dominated with pseudo second-order kinetic model and the high adsorption and degradation capacity of MB in dark on composite TiO_2/C is due to the high surface area porous carbon matrix in the composites. However, composite N-O-TiO_2/C showed the highest photodegradation of MB under visible light due to the optimal anatase/rutile phasejunction, the doping of N species and formation of photoactive oxygen-rich N-O like interstitial/intraband states above the valence band of TiO_2, as well as the rich -OH/-COOH functional groups with superhydrophilic nature of the composite. The photocatalytic performance of the composites can be further improved by optimizing the combinations of surface-attached functional groups and metal/non-metal co-dopants into TiO_2. This study provides a simple one-step approach to produce simultaneously multi-functionalized and co-doped homogeneous metal oxide/carbon composites which can be used for a variety of novel photocatalytic applications.

Acknowledgements

Declaration of Competing Interest

The authors declare no competing financial interest.

Appendix A. Supplementary data

Supplementary data related to this article can be found online at https://doi.org/10.1016/j.jmst.

References

[1] S.K. Loeb, P.J.J. Alvarez, J.A. Brame, E.L. Cates, W. Choi, J. Crittenden, D.D. Dionysiou, Q. Li, G. Li-Puma, X. Quan, D.L. Sedlak, T. David Waite, P. Westerhoff, J.-H. Kim, Environ. Sci. Technol. 53 (2019) 2937-2947.

[2] M. Rochkind, S. Pasternak, Y. Paz, Molecules 20 (2015) 88-110.

[3] Y.-Z. Chen, R. Zhang, L. Jiao, H.-L. Jiang, Coord. Chem. Rev. 362 (2018) 1-23.

[4] W. Sheng, J.-L. Shi, H. Hao, X. Li, X. Lang, Chem. Eng. J. 379 (2020) 122399.

[5] W. Sheng, J.-L. Shi, H. Hao, X. Li, X. Lang, J. Colloid Interface Sci. 565 (2020) 614-622.

[6] A. Meng, L. Zhang, B. Cheng, J. Yu, Adv. Mater. 31 (2019) 1807660.

[7] K. Qi, B. Cheng, J. Yu, W. Ho, Chinese J. Catal. 38 (2017) 1936-1955.

[8] R. Quesada-Cabrera, C. Sotelo-Vazquez, J.A. Darr, I.P. Parkin, Appl. Catal. B: Environ. 160-161 (2014) 582-588.

[9] Y.-H. Chiu, T.-F.M. Chang, C.-Y. Chen, M. Sone, Y.-J. Hsu, Catalysts 9 (2019) 430.

[10] P.S. Basavarajappa, S.B. Patil, N. Ganganagappa, K.R. Reddy, A.V. Raghu, C.V. Reddy, Int. J. Hydrog. Energy 45 (2020) 7764-7778.

[11] E. Han, K. Vijayarangamuthu, J.-s. Youn, Y.-K. Park, S.-C. Jung, K.-J. Jeon, Catal. Today 303 (2018) 305-312.

[12] C. Han, M. Pelaez, V. Likodimos, A.G. Kontos, P. Falaras, K. O'Shea, D.D. Dionysiou, Appl. Catal. B: Environ. 107 (2011) 77-87.

[13] B. Viswanathan, K.R. Krishanmurthy, Int. J. Photoenergy 2012 (2012) 1-10.

[14] J. Low, J. Yu, M. Jaroniec, S. Wageh, A.A. Al-Ghamdi, Adv. Mater. 29 (2017) 1601694.

[15] X. Huang, W. Yang, G. Zhang, L. Yan, Y. Zhang, A. Jiang, H. Xu, M. Zhou, Z. Liu, H. Tang, D.D. Dionysiou, Catal. Today 361 (2021) 11-16.

[16] S. Cravanzola, F. Cesano, F. Gaziano, D. Scarano, Catalysts 7 (2017) 214.

[17] A. Brindha, T. Sivakumar, J. Photochem. Photobiol. A: Chem. 340 (2017) 146-156.

[18] Y. Xu, Y. Mo, J. Tian, P. Wang, H. Yu, J. Yu, Appl. Catal. B: Environ. 181 (2016) 810-817.

[19] D. Zhao, G. Sheng, C. Chen, X. Wang, Appl. Catal. B: Environ. 111-112 (2012) 303-308.

[20] P. Ribao, M.J. Rivero, I. Ortiz, Environ. Sci. Pollut. Res. 24 (2017) 12628-12637.

[21] P. Singh, P. Shandilya, P. Raizada, A. Sudhaik, A. Rahmani-Sani, A. Hosseini-Bandegharaei, Arab. J. Chem. 13 (2020) 3498-3520.

[22] S.-Y. Lee, S.-J. Park, J. Ind. Eng. Chem. 19 (2013) 1761-1769.

[23] U.G. Akpan, B.H. Hameed, J. Hazard. Mater. 170 (2009) 520-529.

[24] X. Chen, L. Liu, P.Y. Yu, S.S. Mao, Science 331 (2011) 746.

[25] S. Dang, Q.-L. Zhu, Q. Xu, Nat. Rev. Mater. 3 (2017) 17075.

[26] H. Luo, Z. Zeng, G. Zeng, C. Zhang, R. Xiao, D. Huang, C. Lai, M. Cheng, W. Wang, W. Xiong, Y. Yang, L. Qin, C. Zhou, H. Wang, Y. Zhou, S. Tian, Chem. Eng. J. 383 (2020) 123196.

[27] X. Zhang, A. Chen, M. Zhong, Z. Zhang, X. Zhang, Z. Zhou, X.-H. Bu, Energy Environ. Sci. 2 (2019) 29-104.

[28] O.M. Yaghi, M. O'Keeffe, N.W. Ockwig, H.K. Chae, M. Eddaoudi, J. Kim, Nature 423 (2003) 705.

[29] H. Li, M. Eddaoudi, M. O'Keeffe, O.M. Yaghi, Nature 402 (1999) 276-279.

[30] H. Wang, Q.-L. Zhu, R. Zou, Q. Xu, Chem 2 (2017) 52-80.

[31] H. Zhang, J. Nai, L. Yu, X.W. Lou, Joule 1 (2017) 77-107.

[32] Z. Wang, J. Huang, J. Mao, Q. Guo, Z. Chen, Y. Lai, J. Mater. Chem. A 8 (2020) 2934-2961.

[33] F. Marpaung, M. Kim, J.H. Khan, K. Konstantinov, Y. Yamauchi, M.S.A. Hossain, J. Na, J. Kim, Chem. Asian J. 14 (2019) 1331-1343.

[34] M.Z. Hussain, A. Schneemann, R.A. Fischer, Y. Zhu, Y. Xia, ACS Appl. Energy Mater. 1 (2018) 4695-4707.

[35] A. Fujishima, X. Zhang, D. Tryk, Surf. Sci. Rep. 63 (2008) 515-582.

[36] M.Z. Hussain, G.S. Pawar, Z. Huang, A.A. Tahir, R.A. Fischer, Y. Zhu, Y. Xia, Carbon 146 (2019) 348-363.

[37] Z. Guo, J.K. Cheng, Z. Hu, M. Zhang, Q. Xu, Z. Kang, D. Zhao, RSC Adv. 4 (2014) 34221-34225.

[38] D.H. Wang, L. Jia, X.L. Wu, L.Q. Lu, A.W. Xu, Nanoscale 4 (2012) 576-84.

[39] M.Z. Hussain, Z. Yang, Z. Huang, Q. Jia, Y. Zhu, Y. Xia, Adv. Sci. (2021) 2100625.

[40] M.Z. Hussain, Z. Yang, B.v.d. Linden, Z. Huang, Q. Jia, E. Cerrato, R.A. Fischer, F. Kapteijn, Y. Zhu, Y. Xia, J. Energy Chem. 57 (2021) 485-495.

[41] M. Dan-Hardi, C. Serre, T. Frot, L. Rozes, G. Maurin, C. Sanchez, G. Férey, J. Am. Chem. Soc. 131 (2009) 10857-10859.

[42] M.Z. Hussain, M. Bahri, W.R. Heinz, Q. Jia, O. Ersen, T. Kratky, R.A. Fischer, Y. Zhu, Y. Xia, Microporous Mesoporous Mater. 316 (2021) 110957.

[43] D.A.H. Hanaor, C.C. Sorrell, J. Mater. Sci. 46 (2011) 855-874.

[44] B.H. Toby, EXPGUI, J. Appl. Cryst. 34 (2001) 210-213.

[45] M.-G. Ju, G. Sun, J. Wang, Q. Meng, W. Liang, ACS Appl. Mater. Interfaces 6 (2014) 12885-12892.

[46] Y.-D. Zhou, Z.-Y. Zhao, Appl. Surf. Sci. 485 (2019) 8-21.

[47] W.-K. Wang, J.-J. Chen, X. Zhang, Y.-X. Huang, W.-W. Li, H.-Q. Yu, Sci. Rep. 6 (2016) 20491.

[48] M.Z. Hussain, B. van der Linden, Z. Yang, Q. Jia, H. Chang, R.A. Fischer, F. Kapteijn, Y. Zhu, Y. Xia, J. Mater. Chem. A 9 (2021) 4103-4116.

[49] L. Shi, D. Benetti, F. Li, Q. Wei, F. Rosei, Appl. Catal. B: Environ. 263 (2020) 118317.

[50] J.R. Pels, F. Kapteijn, J.A. Moulijn, Q. Zhu, K.M. Thomas, Carbon 33 (1995) 1641-1653.

[51] A.C. Ferrari, J. Robertson, Phys. Rev. B 61 (2000) 14095-14107.

[52] S.E. Rodil, Diam. Relat. Mater. 14 (2005) 1262-1269.

[53] C. Di Valentin, E. Finazzi, G. Pacchioni, A. Selloni, S. Livraghi, M.C. Paganini, E. Giamello, Chem. Phys. 339 (2007) 44-56.

[54] B. Bharti, S. Kumar, H.-N. Lee, R. Kumar, Sci. Rep. 6 (2016) 32355.

[55] R. Asahi, T. Morikawa, H. Irie, T. Ohwaki, Chem. Rev. 114 (2014) 9824-9852.

[56] Z. Huang, Z. Yang, M.Z. Hussain, B. Chen, Q. Jia, Y. Zhu, Y. Xia, Electrochim. Acta 330 (2020) 135335.

[57] Z. Huang, Z. Yang, M.Z. Hussain, Q. Jia, Y. Zhu, Y. Xia, J. Mater. Sci. Technol. 84 (2021) 76-85.

[58] L. Szatmáry, S. Bakardjieva, J. Šubrt, P. Bezdička, J. Jirkovský, Z. Bastl, V. Brezová, M. Korenko, Catal. Today 161 (2011) 23-28.

[59] R.S.C. Smart, W.M. Skinner, A.R. Gerson, Surf. Interface Anal. 28 (1999) 101-105.

[60] B. Chen, R. Li, G. Ma, X. Gou, Y. Zhu, Y. Xia, Nanoscale 7 (2015) 20674-20684.

[61] S. Livraghi, M.C. Paganini, E. Giamello, A. Selloni, C. Di Valentin, G. Pacchioni, J. Am. Chem. Soc. 128 (2006) 15666-15671.

[62] X. Chen, C. Burda, J. Am. Chem. Soc. 130 (2008) 5018-5019.

[63] R. Asahi, T. Morikawa, T. Ohwaki, K. Aoki, Y. Taga, Science 293 (2001) 269.

[64] C. Di Valentin, G. Pacchioni, A. Selloni, S. Livraghi, E. Giamello, J. Phys. Chem. B 109 (2005) 11414-11419.

[65] F.M. Hossain, L. Sheppard, J. Nowotny, G.E. Murch, J. Phys. Chem. Solids 69 (2008) 1820-1828.

[66] T. Umebayashi, T. Yamaki, H. Itoh, K. Asai, Appl. Phys. Lett. 81 (2002) 454-456.

[67] A.M.E. Khalil, F.A. Memon, T.A. Tabish, D. Salmon, S. Zhang, D. Butler, Chem. Eng. J. 398 (2020) 125440.

[68] B. Chen, G. Ma, D. Kong, Y. Zhu, Y. Xia, Carbon 95 (2015) 113-124.

[69] T.A. Saleh, M.N. Siddiqui, A.A. Al-Arfaj, Pet. Sci. Technol. 34 (2016) 1468-1474.

[70] M. Pan, X. Lin, J. Xie, X. Huang, RSC Adv. 7 (2017) 4492-4500.

[71] X. Sui, X. Li, L. Chen, G. Li, F. Lin, C. Liu, RSC Adv. 7 (2017) 49220-49226.

[72] D.O. Scanlon, C.W. Dunnill, J. Buckeridge, S.A. Shevlin, A.J. Logsdail, S.M. Woodley, C.R.A. Catlow, M.J. Powell, R.G. Palgrave, I.P. Parkin, G.W. Watson, T.W. Keal, P. Sherwood, A. Walsh, A.A. Sokol, Nat. Mater. 12 (2013) 798-801.

[73] V. Vaiano, O. Sacco, D. Sannino, P. Ciambelli, Appl. Catal. B: Environ. 170-171 (2015) 153-161.